



Current collector design for closed-plenum polymer electrolyte membrane fuel cells

F.A. Daniels ^a, C. Attingre ^b, A.R. Kucernak ^b, D.J.L. Brett ^{a,*}

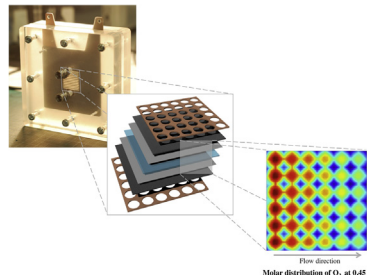
^a Electrochemical Innovation Lab, Department of Chemical Engineering, University College London, Torrington Place, London WC1E 7JE, UK

^b Department of Chemistry, Imperial College London, South Kensington, London SW7 2AZ, UK

HIGHLIGHTS

- A 3D model of a whole planar PEMFC with a closed-plenum flow field is presented.
- Effect of printed circuit board current collector design on transport investigated.
- Parallel channels outperform circular channels with best species distribution.
- Study completed on channel size, current collector material, feed humidification.
- Model predicts key inhibitors of successful operation are flooding and overheating.

GRAPHICAL ABSTRACT



ARTICLE INFO

Article history:

Received 23 July 2013

Received in revised form

26 September 2013

Accepted 12 October 2013

Available online 25 October 2013

Keywords:

Closed-plenum fuel cell
CFD
Flow field design
PCB current collectors
Fuel cell modelling
PEM fuel cell

ABSTRACT

This work presents a non-isothermal, single-phase, three-dimensional model of the effects of current collector geometry in a 5 cm² closed-plenum polymer electrolyte membrane (PEM) fuel cell constructed using printed circuit boards (PCBs). Two geometries were considered in this study: parallel slot and circular hole designs. A computational fluid dynamics (CFD) package was used to account for species, momentum, charge and membrane water distribution within the cell for each design. The model shows that the cell can reach high current densities in the range of 0.8 A cm⁻²–1.2 A cm⁻² at 0.45 V for both designs. The results indicate that the transport phenomena are significantly governed by the flow field plate design. A sensitivity analysis on the channel opening ratio shows that the parallel slot design with a 50% opening ratio shows the most promising performance due to better species, heat and charge distribution. Modelling and experimental analysis confirm that flooding inhibits performance, but the risk can be minimised by reducing the relative humidity of the cathode feed to 50%. Moreover, overheating is a potential problem due to the insulating effect of the PCB base layer and as such strategies should be implemented to combat its adverse effects.

© 2013 Elsevier B.V. All rights reserved.

1. Introduction

Polymer electrolyte membrane fuel cells (PEMFCs) are an attractive alternative for electrical power generation. Their low operating temperature makes them versatile in that they can be used in a variety of applications (e.g. portable, automotive). PEMFCs operate by converting the chemical energy in fuel (of which

* Corresponding author. Tel.: +44 (0)20 7679 3310.

E-mail address: d.brett@ucl.ac.uk (D.J.L. Brett).

URL: <http://www.ucl.ac.uk/electrochemical-innovation-lab>



hydrogen is a particularly good fuel) into electrical power by electrochemically reacting the fuel with oxygen (air); this is associated with the production of water and heat (which can be usefully harvested in certain applications). The core of a PEMFC consists of a membrane electrode assembly (MEA) made of a proton conducting electrolyte (e.g. a perfluorosulfonic acid membrane such as Nafion) sandwiched between two electrodes containing a suitable electrocatalyst. These electrodes are covered with a carbon-based gas diffusion layer (GDL) that facilitates the conduction of electrons and distribution of reactants and products across the electrodes. In conventional fuel cell designs, each MEA is placed between two bipolar plates, which allow for the conduction of current from the MEA to the load and the distribution of the reactants and products to and from the MEA. The bipolar plates also provide the necessary structural stability required by each cell in the stack [1,2].

Given the complexity of the construction and operation of a fuel cell, it is desirable to fully understand the transport phenomena within a given arrangement. Computational tools can be used to determine the need for appropriate reactant transport, water management and heat management through accurate design and operation. Various models can be found in literature for fuel cell operation [3–15], water management [8,16–21], heat management [16,22–25] and bipolar plate design [26–51]. Notable works include the one-dimensional models of Bernardi and Verbrugge, and Springer et al. that were among the first to supply a comprehensive view of steady-state fuel cell operation through coupling of the various transport phenomena [3,10]. Berning et al. presented a three-dimensional model of a PEMFC channel as part of a serpentine flow field design, followed by a parametric study that indicated that contact resistance is a performance limiting factor [4,52].

Understanding the effect of bipolar plate design (flow fields) on fuel cell operation is highly important. The bipolar plate contributes to the majority of the mass of a typical stack and it is known to be costly to fabricate. Optimisation of the flow field is imperative as it has a significant impact on the fuel cell stack performance, geometry, weight and cost. A variety of models exist in literature that investigate the influence of traditional flow field plates such as the serpentine, parallel and pin channel designs [26,27,29,34–46]. Wang et al. have been particularly active in this area [35–45]. They have demonstrated that by altering the channel height within a single serpentine flow field design, sub-rib convection velocities can be achieved that are comparable in magnitude to those in the channel, which results in increased oxygen transportation to the cathode and effective removal of excess water [44]. Further work has shown that through the use of a three-dimensional, two-phase model, serpentine and interdigitated flow fields provide better access of gases to the porous electrodes, which minimises reactant depletion and flooding [41].

Biomimetic flow designs have been proposed as a way to optimise reactant distribution. Wang et al. used computational fluid dynamics to present two different biomimetic designs that showed high flow uniformity and reduced pressure drop across the cell, while maintaining good oxygen distribution and water removal [33]. Advanced flow plate designs have been proposed and demonstrated by Kjelstrup et al. using a nature inspired chemical engineering (NICE) approach that adopts a fractal structure inspired by the human lung [53]. Yi and Nguyen were one of the first research groups to promote the use of an interdigitated design to increase the transportation of reactants in the electrodes under the rib areas [47]. Lobato et al. [28] also demonstrated the use of a three dimensional model on the cathode side for comparison of the parallel, pin and serpentine flow fields in a high temperature fuel cell; the serpentine design gave the best performance due to a more uniform distribution of oxygen and current density across the

active area; however, the model neglects to take into account the problems that are associated with low-temperature PEMFCs [28].

1.1. Self-breathing and closed-plenum fuel cells

The flow fields described above have the common feature of having active advection supply of reactant to the channels such that the channels are enclosed, with flow occurring along their length. However, other geometries exist that have the flow entering above the channel, as shown in Fig. 1.

The self-breathing, also commonly known as the air-breathing, PEMFC has an exposed cathode that is supplied with an oxidant via natural convection (Fig. 1). This configuration is particularly

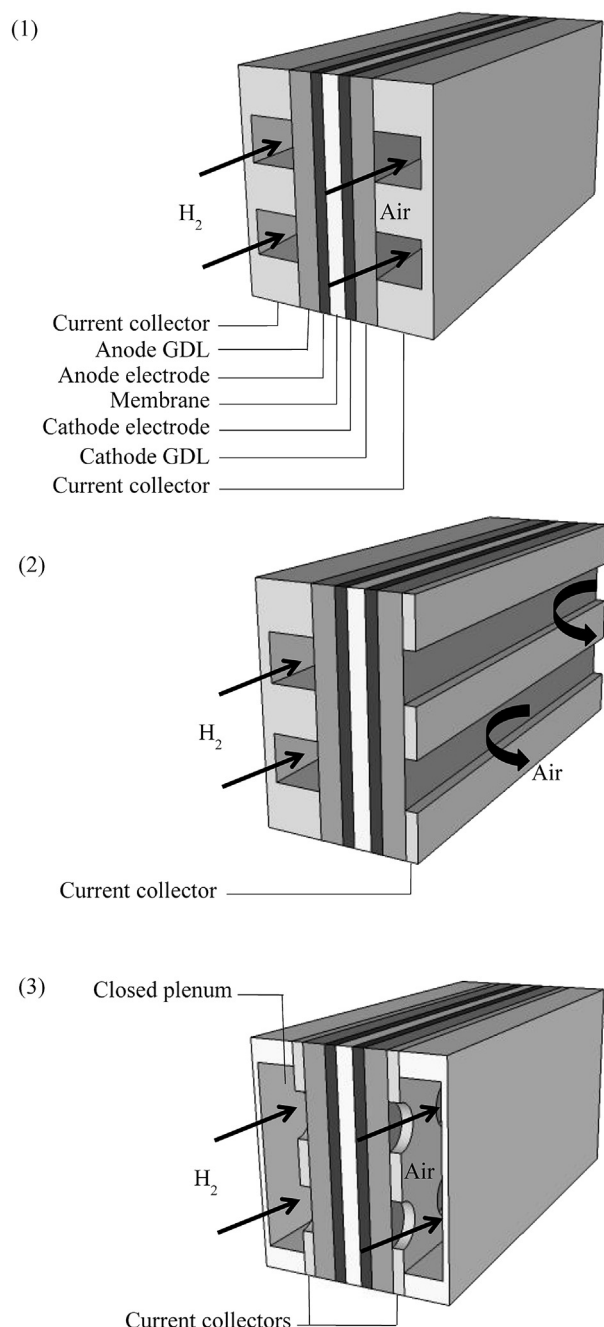


Fig. 1. Three-dimensional representations of: (1) conventional forced-convection, (2) air-breathing and (3) closed-plenum PEMFCs.

advantageous, as it does not require any auxiliary components such as compressors, fans or external humidification to supply the required reactants. Consequently, the performance of a self-breathing fuel cell system is not affected by the parasitic power loss associated with powering a blower. Moreover, the lack of auxiliary equipment means that the size of the self-breathing system may be smaller, making it an attractive design for small, portable devices.

Ziegler et al. was one of the earliest works to demonstrate a self-breathing planar PEMFC with fully coupled transport phenomena through the use of a two-dimensional model [51]. The results indicate that species transportation is a significant issue as the oxygen under the rib is consumed rapidly and the rib obstructs sufficient removal of water. Schmitz et al. further supported this finding through modelling and experimentation by analysing the effect of channel geometry on the self-breathing planar PEMFC, showing that increasing the channel width had a positive effect on cell performance [32]. Ying et al. also investigated the effect of channel width on air-breathing PEMFCs, demonstrating that the width of the channel has a direct effect on the mass and heat transfer within the cell [48,49]. Rajani et al. and O'Hayre et al. have also used modelling to determine the performance of planar air-breathing PEMFCs [21,30]. However, the maximum power a self-breathing fuel cell can generate is limited by mass and heat transport due to natural convection and the design of the cathode due to the lower transport coefficients of natural convection compared to those of forced convection [30]. They are also prone to flooding, as the removal of water produced at the cathode is solely reliant on evaporation [27,54].

The closed-plenum fuel cell (Fig. 1) introduced in this work provides a potential solution by combining the advantageous properties of the conventional and air-breathing cells described above. It acts by allowing feed supply in a closed-plenum via forced convection over a perforated current collector similar to those in self-breathing fuel cells. Consequently, the performance of the cell is potentially higher as the forced convection supports greater mass and heat transport than that in a self-breathing arrangement. More importantly, the improved performance of the closed-plenum fuel cell allows it to be used in applications other than portable devices that have higher power requirements. The pressure drop across the plenum is lower than that in the channels of a conventional fuel cell, thereby reducing the size of the auxiliary feed supply system. Previous attempts at developing similar configurations of this concept have been demonstrated experimentally by Hogarth et al. and O'Hayre et al. [55,56]. Conversely, the closed-plenum cell is potentially prone to the similar problems demonstrated in self-breathing fuel cells where the current collector inhibits effective transport of reactants, water and heat. Therefore, the appropriate selection of a suitable current collector is essential to its viability.

In addition to high performance, reducing the weight, volume and cost of manufacturing is essential in successfully commercialising PEMFC stacks and making them competitive with existing technologies. Many of these objectives can be met by optimising the bipolar plate through the use of well-chosen materials and design. Although graphite is the traditional choice of bipolar plate material, plates made of this material are costly to manufacture and contribute to the bulk of the PEMFC stack volume and mass. As a result, other materials such as stainless steel sheets and printed circuit boards are being considered for use as bipolar plates.

An alternative approach is to use glass reinforced plastics coated with a conducting layer of, most commonly copper, as a current collector. Such materials are commonly used in printed circuit boards (PCBs). In these materials, lateral electrical conduction in the plane of the copper layer is very high, and through-board

conduction can be introduced by vias or plated through-holes. A major benefit of using PCBs is that the materials and manufacturing processes are well known and comparably inexpensive, making them potentially more cost effective. Printed circuit boards consist of a thin layer of copper placed upon a support layer such as the most commonly used FR4, which is made of epoxy resin and glass fibre matting. PCBs can be manufactured to a range of thicknesses (down to ~0.4 mm) making them advantageous to reduce the volume of a PEMFC stack. Moreover, the copper layer of the PCB can be etched to allow for MEAs to be electrically connected laterally to create a planar stack with cells connected in electrical series along the plane of single boards [56] instead of in the traditional 'sandwich' stack structure, thereby potentially reducing the overall size. There is a growing body of literature on planar stacks, particularly for portable applications [56–63].

The planar design has been demonstrated to be advantageous as compact, thin stacks can be produced that are easy to incorporate in a device. However, to achieve maximum operability, the stack would need to operate within a closed environment with forced convection similar to that of a traditional stack. A closed-plenum would ideally supply forced convection necessary to maintain the operating requirements of this type of stack. Furthermore, the use of a closed-plenum in a planar design is potentially a more efficient, optimised method of the distribution of gases as it provides a common manifold (closed-plenum) that can be used by multiple layers of cells (e.g. using one manifold to supply gases to two adjacent layers of anodes or cathodes). By utilising both concepts (i.e. a closed-plenum and a planar arrangement of cells), issues of performance limitations and the size of the fuel cell system can be addressed more successfully.

In this paper, a modelling study is presented to determine the effect of current collector design on the performance of a planar PEMFC with forced convection delivered via a closed plenum across the current collector. Very little literature exists on the use of computational modelling to determine PEM fuel cell performance based on the use of PCBs. Furthermore, existing models focussing on the use of air-breathing systems with PCB current collectors are currently limited to two-dimensional representations, which fail to register potential features that are influential performance limiting factors in three-dimensional models. The model presented here is a representation of a full-sized PEMFC in order to gain a comprehensive perspective of the operation of a whole cell, rather than an estimation of a single channel based on symmetry.

2. Model formulation

2.1. Computational domain and model assumptions

A three-dimensional, steady-state, non-isothermal, single-phase model was produced with two different flow field designs. Each model consists of a 5 cm² active area of an MEA placed between two PCB current collectors with the same flow field design. Furthermore, all of the various configurations in this work are modelled based on an active area of 5 cm².

Two designs were selected for investigation: a flow field with parallel slot perforations and one with circular hole perforations (Fig. 2). These two designs were selected based on promising experimental literature published by Bussajarn et al. [64]. The following base-case geometries were selected for investigation and comparison: the parallel slot flow field consists of 11 parallel slot channels with a channel and rib width of 1 mm each. The circular hole flow field consists of 36 circular hole channels with a diameter of 3 mm and space of 0.7 mm between each channel. Gases flow through a plenum area on the rear of the current collector. Fig. 3 shows a detailed three-dimensional representation of the various

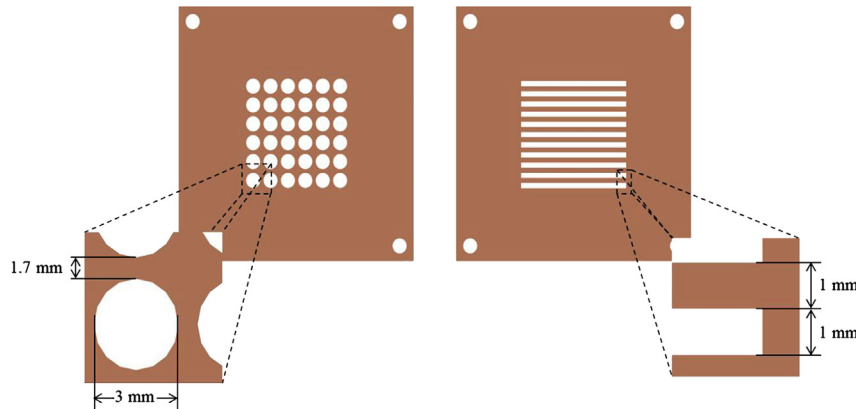


Fig. 2. Visual representation of the flow field plate designs with circular hole (left) and parallel slot (right) perforations.

layers of the cell that are included in the model. For reference purposes in this work, the cell width is the measurement of the cell in the y -direction and the cell length indicates the length of the cell in the x -direction.

Each model takes into account key transport phenomena: (i) multi-component diffusion through the porous gas diffusion and catalyst layers; (ii) convection of reactant gases across the gas channels; (iii) conduction of electrons through the gas diffusion and catalyst layers; (iv) migration of protons across the membrane; (v) water flux across the membrane; (vi) electrochemical reaction within the catalyst domains; (vii) heat transport via conduction and convection within the fuel cell.

These transport properties are determined by using the Maxwell–Stefan equation for multi-component diffusion, the Navier–Stokes equation for momentum transport, the Butler–Volmer and Tafel equations for electrochemical reactions and a modified Maxwell–Stefan equation based on the chemical potential for water flux across the membrane.

To reduce computational cost, several assumptions are considered: (i) operation of the fuel cell is under steady-state conditions; (ii) reactants are compressible ideal gases and are fully saturated with water vapour; (iii) flow in the fuel cell is laminar; (iv) the membrane is impermeable to reactant gases; (v) the water vapour in the electrodes is at equilibrium with that in the membrane; (vi) the anode and cathode operate at atmospheric pressure; as a result,

convection of water within the membrane due a pressure gradient is negligible; (vii) contact losses between electrical components are not considered in the model; (viii) materials are isotropic and homogeneous; (ix) effects of cell compression on the MEA are not considered in this model.

2.2. Governing equations

2.2.1. Flow channels

The ideal gas flow within each set of flow distribution channels is expressed by the momentum balance using the Navier–Stokes equation

$$\rho(\mathbf{u} \cdot \nabla)\mathbf{u} = \nabla \cdot \left[-p\mathbf{I} + \mu(\nabla\mathbf{u} + (\nabla\mathbf{u})^T) - \frac{2}{3}(\nabla \cdot \mathbf{u})\mathbf{I} \right] \quad (1)$$

where \mathbf{u} is the gas velocity (m s^{-1}), ρ is the gas density (kg m^{-3}), p is the pressure (Pa), and μ is the dynamic viscosity of the gas mixture ($\text{kg m}^{-1} \text{s}^{-1}$). Continuity within the channels is provided by

$$\nabla \cdot (\rho\mathbf{u}) = 0. \quad (2)$$

Species mass transport is described by the Maxwell–Stefan equation in the flow channels. Hydrogen and water are the species in the anode. Oxygen, nitrogen and water are the species in the cathode.

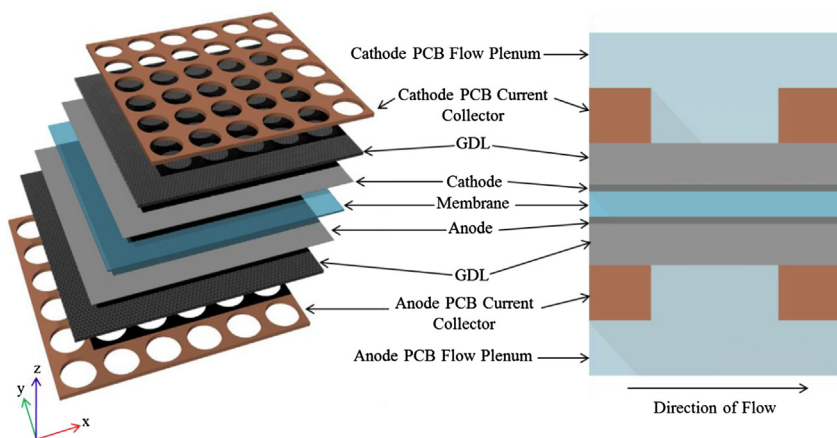


Fig. 3. A representation of the 5 cm^2 PEM fuel cell with the circular hole flow field. The three dimensional picture (left) shows the components of the cell that are modelled with a cross-sectional view in the xz -plane that includes the flow plenum (right).

$$\nabla \cdot \left(\omega_i \rho \mathbf{u} - \rho \omega_i \sum_{j=1}^k \tilde{D}_{ij} \left(\frac{M}{M_j} \left(\nabla \omega_j + \omega_j \frac{\nabla M}{M} \right) + (x_j - \omega_j) \frac{\nabla p}{p} \right) \right) = 0 \quad (3)$$

where ω is the mass fraction, x is molar fraction, M is the molecular mass (kg mol^{-1}), R is the universal gas constant ($8.314 \text{ J mol}^{-1} \text{ K}^{-1}$), D_{ij} is the binary diffusion coefficient of species i in j ($\text{m}^2 \text{ s}^{-1}$), and T is the operating temperature of the cell. The gases are assumed to be ideal and can be expressed by the following equation

$$\rho = \left(\sum_i x_i M \right) \frac{p}{RT}. \quad (4)$$

The following mass balance applies for the respective species in the anode and cathode

$$\sum \omega_i = 1 \quad (5)$$

which is used to obtain the mass fraction of water at the anode and nitrogen at the cathode.

Binary diffusion coefficients are calculated based on the reference value obtained at a specific temperature and atmospheric pressure. The values used in the model can be obtained from

$$D_{ij} = D_{ij}(T_0, P_0) \frac{p_0}{p} \left(\frac{T}{T_0} \right)^{1.5}. \quad (6)$$

The content of water vapour within the gaseous streams is assumed to be saturated. The saturation pressure of water vapour can be approximated using [10]

$$\log_{10} P_{\text{sat}} = -2.1794 + 0.02953 T - 9.1837 \cdot 10^{-5} T^2 + 1.4454 \cdot 10^{-7} T^3 \quad (7)$$

where the molar fraction of water in the gaseous stream can be expressed by

$$x_{\text{H}_2\text{O}} = \frac{P_{\text{sat}}}{P}. \quad (8)$$

The mass and momentum transport equations are coupled via the local velocity vector, \mathbf{u} , and the bulk density, ρ .

2.2.2. Gas diffusion and catalyst layers

In the porous gas diffusion catalyst layers, the flow is obtained from a modified version of the Navier–Stokes equation, the Brinkman equation, which takes into account flow through the porous material, including any shear stresses present

$$\left(\frac{\mu}{\kappa} + Q \right) \mathbf{u} = \nabla \cdot \left[-p \mathbf{I} + \frac{\mu}{\varepsilon} (\nabla \mathbf{u} + (\nabla \mathbf{u})^T) - \frac{2}{3} (\nabla \cdot \mathbf{u}) \mathbf{I} \right] \quad (9)$$

where ε is the GDL porosity and κ is the GDL permeability (m^2). Similarly, continuity is given by:

$$\nabla \cdot (\rho \mathbf{u}) = 0 \quad (10)$$

and by Equation (11) in the catalyst layer:

$$\nabla \cdot (\rho \mathbf{u}) = Q \quad (11)$$

where Q represents the change in momentum due to the electrode reactions (consumption and production of species).

The Maxwell–Stefan equation is used for the channels to quantify the mass transport of each species.

$$\nabla \cdot \left(\omega_i \rho \mathbf{u} - \rho \omega_i \sum_{j=1}^k \tilde{D}_{ij} \left(\frac{M}{M_j} \left(\nabla \omega_j + \omega_j \frac{\nabla M}{M} \right) + (x_j - \omega_j) \frac{\nabla p}{p} \right) \right) = R_i \quad (12)$$

R_i is the reaction rate of species i in the catalyst area. The reaction rate for each species is shown below. At the anode, where only hydrogen is consumed, the source term for water is zero. Species transport in the gas diffusion layers is also determined using Equation (3).

$$R_{\text{H}_2} = -\frac{M_{\text{H}_2}}{2F} i_a \quad (13)$$

$$R_{\text{H}_2\text{O},a} = 0. \quad (14)$$

At the cathode, oxygen is consumed at the catalyst surface and water is produced

$$R_{\text{O}_2} = -\frac{M_{\text{O}_2}}{4F} i_c \quad (15)$$

$$R_{\text{H}_2\text{O},c} = \frac{M_{\text{H}_2\text{O}}}{2F} i_c. \quad (16)$$

2.2.3. Electrochemical equations

The current in a PEM fuel cell has both electronic and ionic components. Electrons produced at the anode travel through the solid conductive layers of the cell to the cathode where they are consumed in the cathodic reaction. The ionic current is formed from the protons that migrate across the membrane. The following charge balances, based on Ohm's law, are used in the model to describe both types of current for the electronic and membrane components respectively

$$\nabla(-\sigma_s \nabla \cdot \phi_s) = S_s \quad (17)$$

$$\nabla(-\sigma_m \nabla \cdot \phi_m) = S_m \quad (18)$$

where σ is the conductivity (S m^{-1}), ϕ is the phase potential and S is the current source (A m^{-3}).

The source terms above are governed by the electrochemical reactions

$$\text{Anode : } S_m = i_a \text{ and } S_s = -i_a \quad (19)$$

$$\text{Cathode : } S_m = i_c \text{ and } S_s = -i_c. \quad (20)$$

The electrochemical reactions in the catalyst layers involve the production or consumption of species in order to produce the electronic current. A linear form of the Butler–Volmer equation is used to determine the current at the anode due to the fast kinetics of the anode reaction [12]. The cathode reaction, which generally has slow reaction kinetics, is given by the Tafel equation for the anode and cathode respectively

$$i_a = a i_{0,a}^{\text{ref}} \left(\frac{C_{\text{H}_2}}{C_{\text{H}_2,\text{ref}}} \right)^{0.5} \left(\frac{\alpha_a + \alpha_c}{RT} F \eta \right) \quad (21)$$

$$i_c = -ai_{0,c}^{\text{ref}} \left(\frac{C_{\text{O}_2}}{C_{\text{O}_2,\text{ref}}} \right) \exp \left(-\frac{\alpha_c}{RT} F\eta \right) \quad (22)$$

where η is the cell overpotential, a is the catalyst surface area, $i_{0,a}^{\text{ref}}$ and $i_{0,c}^{\text{ref}}$ are the exchange current densities for the anode and cathode respectively and $C_{\text{H}_2,\text{ref}}$ and $C_{\text{O}_2,\text{ref}}$ are the reference concentrations hydrogen and oxygen respectively.

The equilibrium potential is expressed by the Nernst equation [4]

$$E_{T,p}^0 = E^0 + \frac{\Delta S}{nF} (T - T^0) + \frac{RT}{nF} \left[\ln p_{\text{H}_2} + \frac{1}{2} \ln p_{\text{O}_2} \right] \quad (23)$$

where ΔS is the change in entropy, n is the number of electrons, p is the partial pressure of the gaseous species and E_0 is the standard reversible potential given by

$$E^0 = \frac{\Delta G^0}{nF} \quad (24)$$

ΔG^0 is the Gibbs free energy of the fuel cell reaction. Equation (24) can be simplified into the following at atmospheric pressures [65]

$$E_{T,p}^0 = 0.0025 T + 0.2329. \quad (25)$$

2.2.4. Heat transport equations

Heat transport by conduction and convection is given by

$$\rho c_p u \cdot \nabla T = \nabla \cdot (k \nabla T) + Q \quad (26)$$

where c_p is the specific heat capacity of the fluid ($\text{J kg}^{-1} \text{K}^{-1}$) and k is the thermal conductivity ($\text{W m}^{-1} \text{K}^{-1}$). The heat source, Q , is the sum of the heat generated from the electrochemical reactions, activation energy losses and Joule heating. The reaction heat generated at the anode is small in comparison to that of the cathode, and is considered negligible in this model. The heat generated at the cathode is determined by Ref. [4]:

$$Q_c = \left(\frac{T(-\Delta S_c)}{4F} + \eta_{\text{act}} \right) i_c. \quad (27)$$

2.2.5. Water transport across the membrane

The transport of water within the membrane is an important phenomenon that contributes to the successful performance of the cell. The movement of water between the cathode and anode occurs via electroosmotic drag from the anode to the cathode, back diffusion from the cathode to the anode and convective flux due to the pressure difference between the two electrodes. A plethora of models have been developed in literature to describe this process within a particular system. The most commonly used model is based on the approach of Springer et al. [10]. Their model describes the flux of water across the membrane based on a comprehensive set of analytical expressions. However, other models have analysed the movement of water based upon the chemical potential within the membrane. This method allows for a greater understanding of the transport phenomena as it takes into account all the interactions between the membrane ionic species, protons and water molecules.

For the purposes of this model, a similar approach to that of Ziegler et al. has been used to capture the effect of water movement within the membrane [51]. The membrane consists of three

species: water, protons and the sulfonic acid groups (RSO) in the Nafion polymer. The transport of protons is fully described by Equation (18). Moreover, the net balance of water in the membrane is determined using a modified version of the Maxwell–Stefan diffusion equation [51]

$$\nabla \cdot \left(-\rho_m \omega_i \sum_{j=1}^k \tilde{D}_{ij} \left(\frac{M_m}{M_j} \left(\nabla \omega_j + \omega_j \frac{\nabla M_m}{M_m} \right) + I_{\text{drag}} \right) \right) = 0 \quad (28)$$

where ρ_m represents the density of the membrane and M_m represents the total molar mass of the membrane. Density, ρ_m , is given by

$$\rho_m = \frac{M_m P}{R T} \quad (29)$$

The mass, M_m , can be defined as

$$M_m = M_{\text{RSO}} x_{\text{RSO}} + M_{\text{H}_2\text{O}} x_{\text{H}_2\text{O}} \quad (30)$$

The flux vector I_{drag} is used to evaluate the movement of water from the anode to the cathode due to electroosmotic drag and is approximated by Ref. [51]

$$I_{\text{drag}} = M_{\text{H}_2\text{O}} n_{\text{drag}} \sigma_m F^{-1} \nabla_z \phi_p \quad (31)$$

The electroosmotic drag is directly related to the number of molecules of water dragged per proton across the membrane, n_{drag} , the membrane conductivity, σ_m , and the ionic potential, ϕ_m . The electroosmotic drag coefficient n_{drag} is estimated by Ref. [10]

$$n_{\text{drag}} = \frac{2.5\lambda}{22} \quad (32)$$

The water content of the membrane, λ , indicates the number of water molecules present in the membrane. In order to ensure that the membrane has a high conductivity, the membrane must be sufficiently humidified. The water content is directly dependent on the activity of water at the interfaces between the membrane and the electrodes

$$\lambda = Za \quad (33)$$

where the activity of water is deduced from

$$a = \frac{x_{\text{H}_2\text{O}} P}{P_{\text{sat}}} \quad (34)$$

In this model, the membrane humidity and the activity of water are assumed to be linearly dependent.

The water content, λ , in the membrane is approximated using

$$\lambda = \frac{x_{\text{H}_2\text{O}}}{1 - x_{\text{H}_2\text{O}}} \quad (35)$$

The membrane conductivity is governed by the local humidity [51]

$$\sigma_m = (0.5139 \lambda - 0.326) \exp \left[1286 \left(\frac{1}{303} - \frac{1}{T} \right) \right] \quad (36)$$

The diffusivity of water in the membrane is also linked to the membrane humidity and can be ascertained from

$$D_w = D_w^0(T_0) \cdot \lambda \exp \left[-\frac{E_w^A}{R} \left(\frac{1}{T} - \frac{1}{T_0} \right) \right] \quad (37)$$

where D_w is the diffusion coefficient of water in the membrane, D_w^0 is the diffusion coefficient of water in the electrolyte at the reference temperature of 298 K, λ is the humidity in the membrane and E_w^A is the activation energy [51].

The mass fraction of water in the catalyst layer at the interface between the membrane and the cathode is [51]

$$\begin{aligned} w_{\text{H}_2\text{O}}^c = & \left\{ M_{\text{H}_2\text{O}} M_{\text{RSO}} P_{\text{sat}} w_{\text{H}_2\text{O}}^m [M_{\text{O}_2} (w_{\text{O}_2} - 1) - M_{\text{N}_2} w_{\text{O}_2}] \right\} \\ & \cdot \left(M_{\text{O}_2} \left\{ M_{\text{N}_2} M_{\text{RSO}} P_{\text{sat}} w_{\text{H}_2\text{O}}^m + M_{\text{H}_2\text{O}} [Z M_{\text{N}_2} P_{\text{ref}} \right. \right. \\ & \left. \left. \cdot (w_{\text{H}_2\text{O}}^m - 1) - M_{\text{RSO}} P_{\text{sat}} w_{\text{H}_2\text{O}}^m] \right\} \right)^{-1} \end{aligned} \quad (38)$$

The mass fraction of water in the membrane at the cathode-membrane interface is [51]

$$\begin{aligned} w_{\text{H}_2\text{O}}^{m,c} = & \left(Z M_{\text{H}_2\text{O}} M_{\text{N}_2} M_{\text{O}_2} P w_{\text{H}_2\text{O}}^c \right) \cdot \left(M_{\text{N}_2} M_{\text{O}_2} M_{\text{RSO}} P_{\text{sat}} w_{\text{H}_2\text{O}}^c \right. \\ & \left. + M_{\text{H}_2\text{O}} \left\{ M_{\text{N}_2} M_{\text{RSO}} P_{\text{sat}} w_{\text{O}_2} + M_{\text{O}_2} [Z M_{\text{N}_2} P w_{\text{H}_2\text{O}}^c \right. \right. \\ & \left. \left. - M_{\text{RSO}} P_{\text{sat}} (w_{\text{H}_2\text{O}}^c + w_{\text{O}_2} - 1)] \right\} \right)^{-1} \end{aligned} \quad (39)$$

2.2.6. Boundary conditions & initial values

Anode: Inlet velocities were calculated based on the stoichiometric ratio, the cell active area, the inlet pressure and cross-sectional area [4]

$$u_{\text{in},a} = \zeta_a \frac{i}{2F} A_{\text{MEA}} \frac{1}{x_{\text{H}_2,\text{in}}} \frac{RT}{p_{a,\text{in}}} \frac{1}{A_{\text{inlet}}} \quad (40)$$

The mass fraction of hydrogen and temperature are

$$w_{\text{H}_2} = w_{\text{H}_2,\text{in}} \quad (41)$$

$$T_{\text{in}} = T_0 \quad (42)$$

At the outlet, convective flux conditions and atmospheric pressure were assumed. To ensure stability of the model, mass fractions were specified at the anode-membrane interface.

For hydrogen [51]

$$w_{\text{H}_2} = 1 - \frac{M_{\text{H}_2\text{O}} M_{\text{RSO}} P_{\text{sat}} w_{\text{H}_2\text{O}}^m}{[Z M_{\text{H}_2} M_{\text{H}_2\text{O}} P (1 - w_{\text{H}_2\text{O}}^m) + M_{\text{RSO}} P_{\text{sat}} w_{\text{H}_2\text{O}}^m (M_{\text{H}_2\text{O}}^m - M_{\text{H}_2})]} \quad (43)$$

For water in the membrane at the interface [51]

$$\begin{aligned} w_{\text{H}_2\text{O}}^{m,a} = & \left(Z M_{\text{H}_2} M_{\text{H}_2\text{O}} P_{\text{ref}} w_{\text{H}_2\text{O}}^a \right) \cdot \left\{ M_{\text{H}_2} M_{\text{RSO}} P_{\text{sat}} w_{\text{H}_2\text{O}}^a \right. \\ & \left. + M_{\text{H}_2\text{O}} [Z M_{\text{H}_2} P w_{\text{H}_2\text{O}}^a + M_{\text{RSO}} (P_{\text{sat}} - P_{\text{sat}} w_{\text{H}_2\text{O}}^a)] \right\}^{-1} \end{aligned} \quad (44)$$

Cathode: The inlet velocity at the cathode is [4]

$$u_{\text{in},c} = \zeta_c \frac{i}{4F} A_{\text{MEA}} \frac{1}{x_{\text{O}_2,\text{in}}} \frac{RT}{p_{c,\text{in}}} \frac{1}{A_{\text{inlet}}} \quad (45)$$

The inlet mass fractions and temperature are

$$w_{\text{O}_2} = w_{\text{O}_2,\text{in}} \quad (46)$$

$$w_{\text{H}_2\text{O}} = w_{\text{H}_2\text{O},\text{in}} \quad (47)$$

$$T_{\text{in}} = T_0. \quad (48)$$

Likewise, convective flux and atmospheric pressure are assumed at the outlet.

All other exterior boundaries are specified as walls with no-slip and no-flux mass conditions.

3. Model solution and experimental validation procedure

3.1. Computational solution

The three-dimensional representations of each design model were constructed and solved in COMSOL Multiphysics 4.2a, a computational fluid dynamics package. COMSOL provides a set of general purpose partial differential equations that can be applied in a finite-volume element analysis.

A thorough mesh sensitivity analysis was performed in order to assure the accuracy of the results reported. A series of structured meshes with an increasing number of mesh elements were created for each design to determine a mesh-independent solution. The model was solved using each mesh, and the values of current density were compared at 0.4 V and 0.6 V. It was found that 38,330 elements and 30,310 elements were needed for the parallel slot and circular hole designs respectively, in order to obtain a solution that was independent of the geometry of the mesh. Where indicated, the limiting current density was defined by the model's inability to converge at the given voltage used during the solution procedure.

The solution procedure was divided into a sequential process of first solving for the mass and momentum transport in the flow channels, GDL and catalyst layers to provide initial values for the final solution of all the transport phenomena and to promote solution stability. A multi-frontal massively parallel sparse direct solver (MUMPS) was used to solve the given set of PDEs assigned to the geometry across a range of 0.5 V–0.9 V to produce a polarisation curve. MUMPS was chosen, as it is the default solver recommended by the solution program. Furthermore, the solver reduces computational cost by minimising the internal memory used during the solution procedure. The time taken to complete a full sweep of the VI curve was 6032 s and 4623 s for the parallel slot and circular hole designs respectively using a PC with an Intel Xeon W3565 Quad Core Processor at 3.2 GHz with 24 GB RAM.

3.2. Model parameters

Tables 1 and 2 show the geometrical, physical and operating constants used in all versions of the model considered in this work. The values were selected based on well-known values used in literature and those obtained from the physical representations of the single cells and materials used.

3.3. Experimental evaluation

The model was experimentally validated with a 5 cm² cell using parallel slot channel PCB current collectors in a standardised test cell. The purpose of the experimental testing was to determine the potential effects of two-phase water transport that could not be captured by the model. The cell was tested using a Scribner 850e test station, which includes cell humidification and a load for polarisation measurements. The cell was heated using cartridge heaters located in the cell housing controlled using a PID controller (Omega CN7500). The membrane electrode assembly (MEA) was constructed in-house using a Nafion 212 membrane and electrodes cut from Alfa Aesar 45,372 hydrogen electrode/reformate cathode sheets into 5 cm² with a catalyst loading equivalent to 0.543 mg cm⁻². The MEA was hot pressed at 170 °C and 31.3 atm for

Table 1
List of parameters and constants.

Property	Value
Active area, A	5 cm ²
Temperature, T_0	80 °C
N_2/O_2 ratio	79/21
Inlet mass fraction H_2 , w_{H_2}	0.53
Operation pressure, anode/cathode, P_0	1 atm/1 atm
Anode exchange current density, $i_{0,a}$	10^5 A m^{-2}
Cathode exchange current density, $i_{0,c}$	1 A m^{-2}
Cell length, L	2.23 cm
PCB plate thickness, t_{PCB}	0.4 mm
GDL thickness, t_{GDL}	300 μm
Electrode thickness, t_e	50 μm
Membrane thickness, t_m	183 μm
Copper thickness, t_{Cu}	35 μm
Flow plenum thickness, t_{FP}	0.4 mm
Porosity, ϵ (11)	0.4
Electronic conductivity, σ (4)	6000 S m ⁻¹
GDL permeability, κ_{GDL}	$1.18 \times 10^{-11} \text{ m}^2$
Faraday's constant, F	96,485 C mol ⁻¹
Anode transfer coefficient, α_a	1
Cathode transfer coefficient, α_c	0.5
Equivalent weight of polymer, M_{RSO} (7)	1.1 kg mol ⁻¹
Molar mass of hydrogen, M_{H_2} (51)	0.002 kg mol ⁻¹
Molar mass of oxygen, M_{O_2} (51)	0.032 kg mol ⁻¹
Molar mass of water, M_{H_2O} (51)	0.018 kg mol ⁻¹
Molar mass of nitrogen, M_{N_2} (51)	0.028 kg mol ⁻¹
Feed/air stoichiometric coefficient	1.5/1.5
Activation energy, E_a^A (51)	20.25 kJ mol ⁻¹
Diffusion coefficient for electrolyte, D_w^0 (51)	$0.55 \times 10^{-11} \text{ m}^2 \text{ s}^{-1}$
Constant of proportionality, Z (51)	14
Thermal conductivity of POCO graphite (2)	95 W m ⁻¹ K ⁻¹

3 min. It was conditioned prior to testing for 1 h at subsequent current loadings of 100 mA cm⁻², 300 mA cm⁻², 400 mA cm⁻² and 500 mA cm⁻², at which point the voltage at each current density showed no sign of further improvement. The closed plenum of the cell was created by placing a silicon gasket of thickness 1 mm between the back of the PCB current collector and the end plate. A window of 5 cm² was cut into the gasket to create the 'closed plenum' that aligns over the channels of the PCB. The cell was tested using the same operating conditions provided in Table 1. The model was adjusted to take into account the geometrical features and the material properties of the cell tested for accurate comparison between model and experimental data (Table 3).

4. Results and discussion

4.1. Influence of design on cell performance

The model was used to generate polarisation curves for the fuel cell using both closed-plenum designs in order to establish the possible effects of flow field geometry. Concurrently, the model was also used to ascertain the effects of closed plenum design and material on performance in comparison to that of conventional POCO graphite and PCB current collectors with forced convection, as depicted in Fig. 1(a). The average current density was estimated

Table 2
Binary diffusion coefficients [4].

Property	Value (m ² s ⁻¹)	Reference temperature, T_0 (K)
$D_{H_2-H_2O}$	9.15×10^{-5}	307.1
$D_{O_2-N_2}$	2.2×10^{-5}	293.2
$D_{O_2-H_2O}$	2.82×10^{-5}	308.1
$D_{N_2-H_2O}$	2.56×10^{-5}	307.5

Table 3
Geometry parameters used in model for experimental evaluation.

Property	Value
Cell plenum	1 mm
Current collector thickness	0.4 mm
Membrane thickness	50 μm

by evaluating the integral of the local current within the anode over the MEA active area.

As can be seen in Fig. 4, VI curves for both closed-plenum designs follow a nearly identical trend throughout the current density range. Each exhibit a significant loss of performance due to activation overpotentials within the lower current density range of 0 A cm⁻²–0.3 A cm⁻². The contribution of the flow field design on the Ohmic losses is relatively minimal as there is a very little disparity between the VI curves for each design.

Of particular note is the effect of channel geometry on the performance at higher current densities. As previously mentioned, the current density output of the closed-plenum designs between 0.45 V and 0.65 V is similar and the contribution of the design can be considered negligible. However, the cell can perform over a greater range of current densities when using a parallel slot flow field (Fig. 4). Between 0.4 V and 0.45 V, the cell experiences very low oxygen concentrations in the GDL and electrode areas and, as a result, reaches its limiting current density. The model also predicts that the circular hole flow field fails to produce current beyond 0.45 V due to oxygen depletion, which is further discussed below. Furthermore, at 0.45 V, the fuel cell produces approximately 2.2% more current per unit of area when using the parallel slot flow field than using the circular hole flow field. Although this is a small difference, the VI curves give a possible indication of the limitation of the cell due to transport mechanisms, specifically at higher current densities where concentration overpotentials are dominant. The current density output of the fuel cell at lower potentials becomes increasingly reliant on the local reactant species, which is directly influenced by the delivery of gases to the porous layers due to the design. Moreover, this is supported by the higher cell performance exhibited at lower potentials when using POCO graphite and PCB with conventional forced convection due to a more uniform distribution of species (Figs. 4 and 5). Furthermore, the

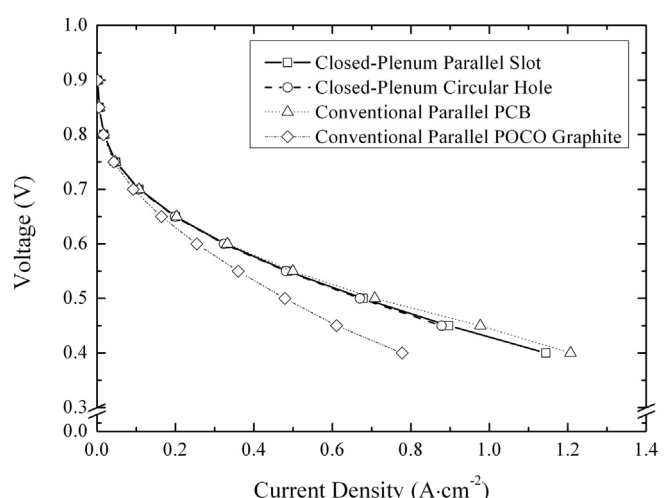


Fig. 4. Polarisation comparison of the (a) parallel slot, (b) circular hole, (c) conventional parallel PCB and (d) conventional parallel POCO graphite flow fields at 80 °C, feed stoichiometries of 1.5 and atmospheric pressure outlet and 100% relative humidity for both inlet feeds.

conventional PCB current collector proves to be advantageous over graphite due to its high electrical conductivity, despite the higher current density exhibited in the cathode of the graphite cell. Based on this initial analysis, the various designs were compared at potentials of 0.45 V, 0.6 V and 0.8 V to gain a better understanding of the local transport mechanisms within the geometry.

The effect of drawing current laterally through the thin copper layer from the porous electrically conductive layers on cell performance was found to be negligible for both closed-plenum current collector designs at all potentials considered. It was found that the dominant contributor to current distribution is the local species concentration. As can be seen in Fig. 6, at 0.6 V, the current density in the cathode in the y -direction along the middle of the cell at $x = 11.15$ mm has a very similar profile to the oxygen mole fraction for both designs. A likely reason that the lateral current conduction does not prominently influence performance in this scenario is due to the relatively small distance over which it has to travel, equivalent to the width of the cell at 22.3 mm. Given that the porous and copper layers have low lateral resistance (calculated as being 0.96 mΩ per square based on a copper layer thickness of 35 μm, a coverage of 50%, and a bulk resistivity of $1.68 \times 10^{-8} \Omega \text{ m}$), any

electrical resistance due to the material properties may be minimal in comparison to other losses in the cell.

The effective distribution of reactants plays an instrumental role in determining the performance of a PEMFC. The mole fractions of the reactant species for the closed-plenum cells steadily decrease along the positive x -direction (direction of reactant flow in the plenum) as it is consumed. At 0.45 V, the mole fraction of hydrogen decreases from 0.54 to a minimum of ~0.38 (parallel slot) and 0.39 (circular hole) indicating that performance limitation due to hydrogen depletion is unlikely during operation. However, it is important to note that there is an appreciable concentration gradient of oxygen along the positive x -direction and negative z -direction due to the cathodic oxygen reduction reaction. The oxygen molar fraction ranges from 0.11 to 2.31×10^{-3} , and 0.023 at 0.45 V when using the parallel slot and circular hole designs, respectively. The local oxygen concentrations reach considerably lower values, potentially subjecting cell operation to the effects of reactant depletion.

The distribution of oxygen within the electrode is greatly influenced by the geometry of the perforated flow field (Fig. 7). Examining the oxygen molar fraction at the interface between the cathode and the membrane, there is a stark contrast between the area under the channels, where the oxygen concentration is high, and under the ribs, where there is a substantially lower amount of oxygen available (there is the same open area ratio of 50% in each design). The diffusion process largely governs transport of oxygen in the cathode under the ribs of the flow field and, as a result, these areas are acutely prone to oxygen depletion. The lack of oxygen within these areas directly affects the local current in the cathode; hence, the cell performance is limited due to the inconsistent current density profile within the cell.

This effect of oxygen depletion is exacerbated as the cell potential decreases along the polarisation curve. At 0.8 V, the local current density is low for the cell using both designs, so there is a very little change in the local oxygen concentration due to low reaction consumption. The molar fraction of oxygen, which decreases to a minimum of approximately 0.058 for both the parallel slot and circular hole designs at 0.6 V, is sufficient to maintain the local electrochemical reaction and would not significantly impede the performance of the fuel cell. However, at 0.45 V, the cathodic

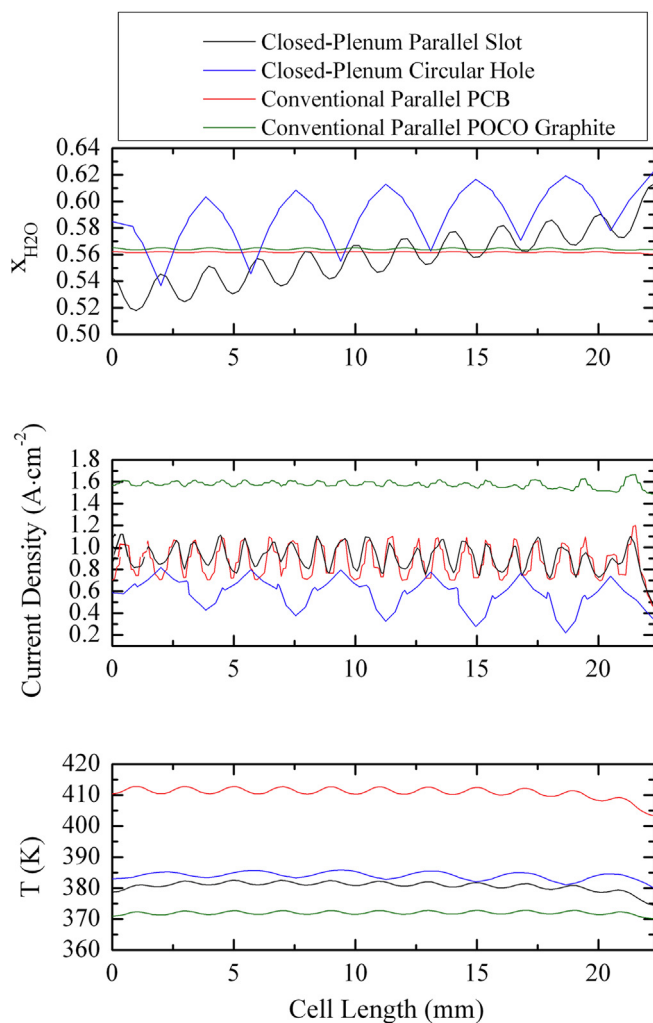


Fig. 5. Comparison of the molar fraction of water, current density and temperature along the length of the cell (x -direction) at 0.45 V for the (a) closed-plenum parallel slot, (b) closed-plenum circular hole flow field configurations, (c) conventional parallel PCB and (d) conventional parallel POCO graphite current collectors.

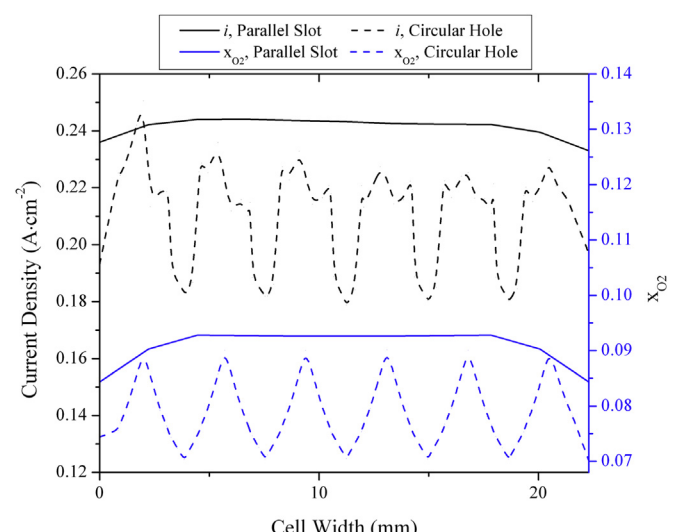


Fig. 6. Lateral current density in the cathode and molar fraction of oxygen along the width of the cell (y -direction) at the centre of the cell ($x = 11.15$ mm) at 0.6 V for the cell using the (a) parallel slot and (b) circular hole PCB current collectors.

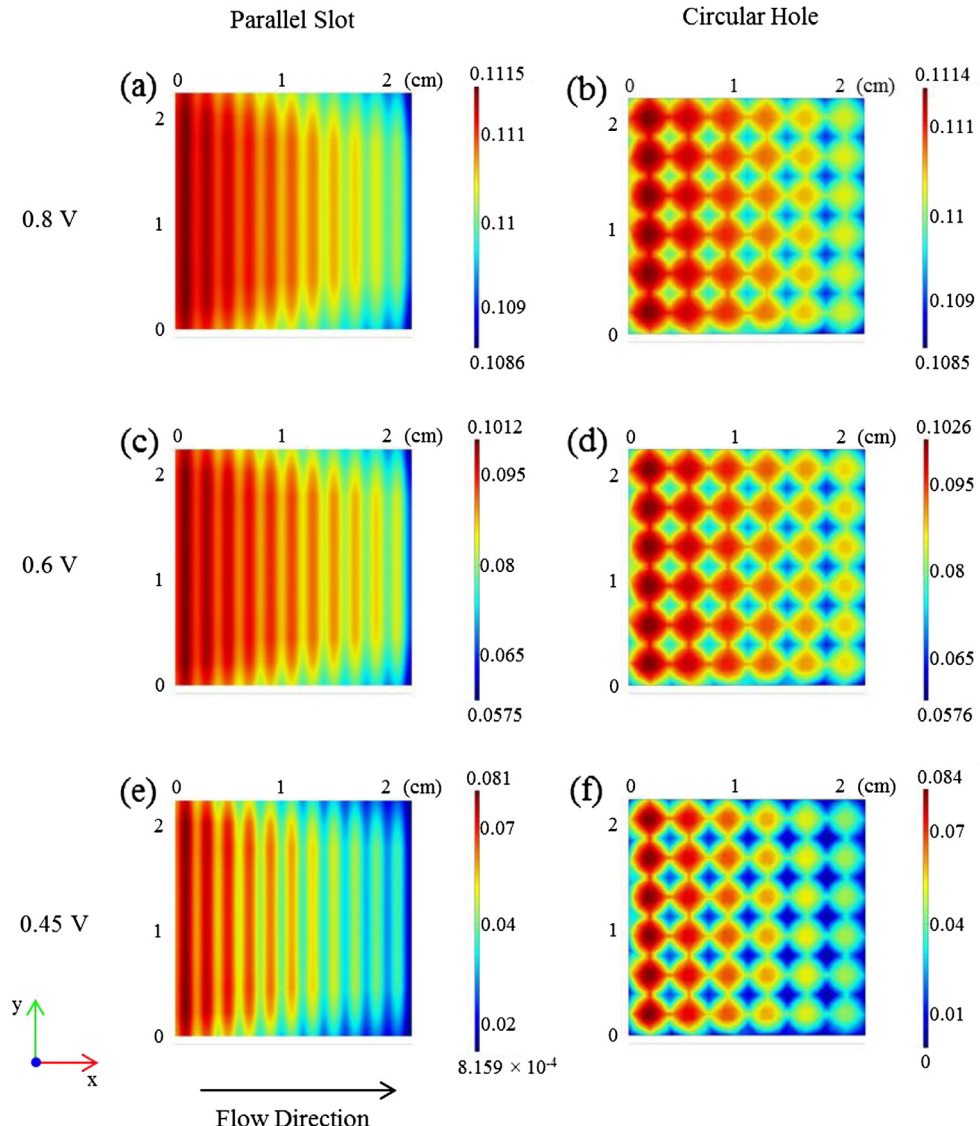


Fig. 7. Oxygen distribution at the cathode-membrane interface for the parallel slot design at (a) 0.8 V, (c) 0.6 V, (e) 0.4 V and the circular hole design at (b) 0.8 V, (d) 0.6 V and (f) 0.45 V. Both channel designs have an opening ratio of 50% for fair comparison.

reaction drives a strong consumption of the oxygen species, leading to depletion under the rib areas. Furthermore, a higher proportion of the active area operates at reduced oxygen concentrations for both flow field designs. Oxygen depletion is further caused by consumption along the length of the closed-plenum cell (Fig. 7). In contrast, the conventional current collectors display a better distribution of species in the catalyst layer due to the forced convection supplied along the length of the channels. The inherent design of conventional parallel flow field implies that each repetitive unit of area under a channel and rib receives the same molar concentration of species delivered by the gases along the length of the cell. The comparison suggests that the delivery and distribution of oxygen in the catalyst layers contributes to increased performance at lower potentials.

The use of the parallel slot flow field is particularly advantageous in comparison to that of the circular hole as there is more uniform distribution of gaseous species within the cell across the range of potentials considered. The smaller area of the ribs allows for the easier supply oxygen and removal of water, which reduces the chances of cell failure due to a lack of efficient mass transport.

The more evenly distributed current profile in the cathode would result in fewer complications due to localised thermal stress and flooding over the lifetime of the cell. In contrast, a large percentage of the cathode exhibits low oxygen content frequently across the potential range considered when using the circular hole channel flow field, which deteriorates in the positive x -direction due to reaction consumption.

Heat is produced within fuel cells due to reversible and irreversible losses such as the entropies of reaction and Ohmic heating. The resulting heterogeneous temperature profile has a significant impact on the overall transport characteristics and is an important criterion for selecting the appropriate design and operating conditions.

The model predicts that the average temperature of the cell rises considerably from 353 K at 0.8 V to a maximum of 381 K and 373 K, 372 K and 412 K at 0.45 V for the parallel slot and circular hole, conventional graphite and conventional parallel PCB designs respectively as current density increases. The highest temperatures are located in the cathode due to the heat from the reaction entropy and the membrane due to its lower ionic conductivity across the

range of potentials investigated for each design. Similarly, the temperature profile along the y -dimension is directly related to the local species concentration and current density. Consequently, hotspots are located under the channels of the flow fields where the cathodic reaction has the most activity. Furthermore, higher temperatures are located closer to the inlet in the positive x -direction due to the higher concentration of reactant species and current density towards the start of the plenum.

Heat removal by mass transport from the electrodes of the closed-plenum designs is limited by the diffusion and convection processes within the porous layers, resulting in the elevated temperatures found in these layers. Comparing the two designs, a greater proportion of the active area when using the circular hole channel flow field operates at higher temperatures, whereas a more uniform distribution of heat is found in the active area when using the parallel slot channels. Moreover, the average temperature of the cathode when using the parallel slot flow field is considerably higher across the range of current densities than its counterpart due to the better distribution of reactants (Fig. 5). Operating at these sustained high temperatures will lead to seriously diminished cell performance due to insufficient hydration of conventional electrolytes. Typically, Nafion membranes are not operated at temperatures above 100 °C at atmospheric pressure as the water necessary for proton conduction evaporates [66]. The decreased water content results in an increased membrane resistance that contributes to high Ohmic losses during operation. Long-term operation at higher temperatures can also result in cell failure due to mechanical deformation as a result of the thermal stresses within the components.

Furthermore, the model suggests that the choice of current collector material has a key influence on cell temperature. The temperature in the cathode ranges from 403 K to 412 K and 370 K to 372 K for the conventional parallel PCB and graphite current collectors respectively. The difference in the ranges of values between the two materials is partially due to the fact that the cell is operating at different current densities for the temperatures considered in Fig. 5. However, literature has demonstrated that elevated temperatures in a cell can be the result of lower thermal conductivity of the material used [45]. Furthermore, the temperature profile found in the cathode when using a graphite current collector follows a similar trend to those presented in literature [45]. Although the thin copper layer of the PCB has a high thermal conductivity, the FR4 support layer, made of epoxy resin and woven glass fibre, has a significantly lower thermal conductivity than that of graphite. Consequently, it effectively acts as an insulator in the cell causing much higher temperatures than those experienced in conventional cells. Furthermore, this observation explains the elevated temperatures exhibited in the conventional parallel PCB cell in comparison to the closed-plenum designs, as the current collector is 0.4 mm thicker than the closed-plenum PCB in order to maintain the same total flow depth. Consequently, PCB current collectors with other support layers that have a higher thermal conductivity could potentially be used as a way to minimise the appearance of higher temperatures in addition to other cooling methods if necessary.

A limitation of the thermal aspect of this model lies in its single-phase nature, which does not account for the removal of heat via evaporation of liquid water in the cell. This process would aid in removal of heat, resulting in lower temperatures than those demonstrated in Fig. 5. More importantly, the higher temperatures observed in both the parallel slot and circular hole channel current collectors are the result of the insulating properties of the FR4 support layer of the PCB.

The water balance of the cell is a key aspect when modelling the transport phenomena as it has a direct effect on the gas compositions and the ionic conductivity of the electrolyte. Transport of

water across the cell occurs via three mechanisms: (i) electroosmotic drag from the anode to the cathode, (ii) back diffusion from the cathode to the anode, and (iii) convection due to a pressure gradient across the membrane. The latter phenomenon has not been considered in this model due to the assumed uniform pressure in the membrane.

The mole fraction and flux of water in the cathode and anode at 0.45 V were compared for both closed-plenum designs. This potential has been specifically chosen for observation as the water content in both electrodes as it shows the greatest differentiation in performance between both designs. The mole fraction of water in the anode increases from 0.463 to 0.616 and 0.468 to 0.609 for the parallel slot and circular hole designs respectively. Likewise, the mole fraction in the cathode fluctuates between a range of 0.518–0.613 and 0.536–0.623 respectively. As the current density increases, the local concentration of water in the cathode increases due to production by the electrochemical reaction and the electroosmotic drag increases as it is directly related to the local current density. Due to the full humidification of the membrane, transport of water from the cathode to the anode is negligible in comparison to that due to electroosmotic drag. Consequently, there is net transport of water across the membrane from the anode to the cathode. Furthermore, this trend was exhibited across the entire range of current densities. In comparison, the mole fraction of water in the cathode for the conventional parallel channel design is relatively uniform across the length of the cell at 0.56 due to the removal of excess water via forced convection of the feed stream.

Although both designs considered here have equal opening ratios (50%), the arrangement of the open channel area within the parallel slot flow field allows for easier transport of excess water from the cathode. The cell shows partial pressures of water higher than the saturation pressure when using both designs, however, there are fewer areas in the cell using the parallel slot design operating at the higher end of the range of partial pressures (Fig. 5). The nature of the ribs between the circular holes prevents easy removal of excess water via diffusion and convection as there is a greater path length between the holes, causing water to accumulate underneath the ribs. The mole fraction of water reaches a maximum of 0.63 and 0.62 in the cathode when using for the circular hole and parallel slot designs respectively indicating that the partial pressure of water vapour is higher than that of the saturation pressure. Consequently, gaseous water would condense to form liquid droplets within the porous layers. More importantly, these areas of supersaturation are mostly found under the ribs of the flow field where transport by diffusion and convection is limited. The formation of water droplets makes the active area prone to the effects of flooding, as there is no effective mechanism present to remove the water such as the advection that is present along the surface of the GDL, as seen in the case of the conventional parallel design. Based on this analysis, operating the cell using fully humidified gases exhibits a high risk of adverse effects on cell performance due to the nature of the design. Therefore, a suitable operating procedure and humidification strategy would need to be designed in order to prevent possible flooding and to prolong the use of the cell.

4.2. Model validation

The model result obtained for the 5 cm² cell using the base case parallel slot channel current collector discussed in Section 2.1 was compared to the experimental data measured from the test cell discussed in Section 3.3 to determine any influence of flooding on cell performance (Fig. 8). The IR-corrected experimental values were used for comparison, as the model does not take into account performance loss due to contact resistance. A good correlation is

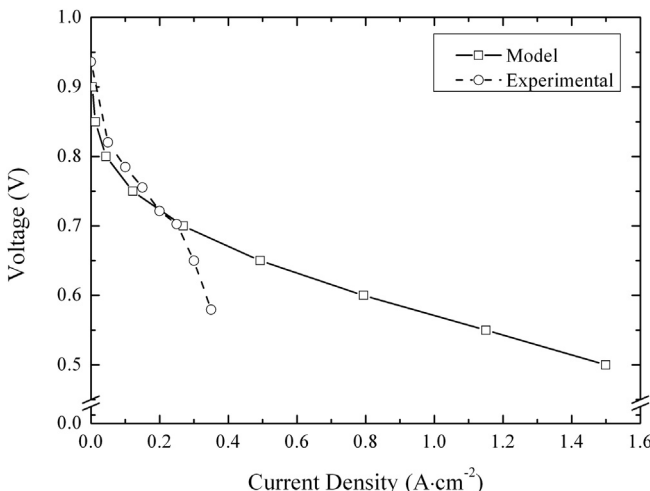


Fig. 8. Comparison of the polarisation curves obtained from the model and experimental evaluation for the closed plenum parallel slot channel PCB current collectors.

observed between the model and experimental results in the range of 0 mA cm^{-2} – 250 mA cm^{-2} , where activation losses are most prevalent.

The experimental values deviate significantly from what the model predicts at current densities greater than 250 mA cm^{-2} and fails to operate past a current density of 350 mA cm^{-2} primarily due to severe mass transport losses due to flooding, which is not captured by the model due to its single-phase nature. During testing, the cell voltage fluctuated considerably between readings and water droplets were observed exiting the cathode outlet of the test cell suggesting severe flooding in the cathode. The presence of excess water in the cell, particularly at the cathode where mass transport losses are often prevalent and detrimental even in conventional cells, indicates that further optimisation is required to balance the humidification required for the cell and water produced at the cathode. Various methods can be employed to minimise the effects of flooding in the cell, including: use of gas feeds with lower humidification, operation at higher stoichiometries and the use of membrane materials that require less humidification. Although the model does not capture the effects of flooding, it does provide a useful insight into the potential performance that the closed plenum fuel cell can achieve with the correct water management tools in place.

4.3. Parametric study of flow field geometry feature size

Three sets of channel dimensions were modelled to determine the effect of changing geometry of both the parallel slot and circular hole designs on cell performance. The dimensions for the parallel slot design used were rib/channel widths of 2 mm/1 mm, 1 mm/1 mm and 1.3 mm/2 mm, which correspond to 33%, 50%, and 62% opening ratios. Circular hole channel diameter dimensions of 2 mm, 3 mm and 4 mm were investigated, which correspond to opening ratios of 31%, 51% and 63% respectively.

[Fig. 9\(a\)](#) shows that increasing the opening ratio of the parallel slot design is positively correlated to an increase in cell performance. In fact, a parallel slot channel current collector with an opening ratio of 33% produces 22.2% less current per unit area at 0.4 V and an opening ratio of 62% yields a gain of 0.25% in comparison to the base case of a 50% opening ratio. However, little improvement is seen between an opening ratio of 50% and 62%. Moreover, there is negligible effect on the cell performance when increasing the opening ratio for a circular hole design. The model

estimates that current densities above 0.6 A cm^{-2} and 0.68 A cm^{-2} cannot be produced by plates with a circular hole opening ratio of 31% and 62% respectively due to mass transport limitations in the cathode ([Fig. 9\(b\)](#)).

Evaluating all of the channel configurations at 0.6 V indicates that the uneven distribution of oxygen is a limitation of cell performance. In [Fig. 10](#), the concentration of oxygen reaches appreciably low values in the areas of the electrodes located under the current collector. The application of the potential field in these areas results in higher reactivity and greater consumption of the oxidant. Comparing the two designs, the circular hole flow field shows better potential for oxygen distribution in the cathode throughout the electrode due to the open area available for gas supply from the plenum. The model demonstrates that an increase in the circular hole opening ratio is positively associated with a more uniform availability of oxygen in the cathode. However, circular hole channels of 2 mm diameter are considerably more prone to oxygen depletion around the edges of the MEA where supply is limited by diffusion through the porous layer. Conversely, a greater proportion of the electrode area when using a parallel slot flow field operates at low oxygen mole fractions for opening ratios of 33% and 62%. The lower presence of oxygen when using a current collector with an opening ratio of 33% is caused by consumption that is not sufficiently replenished due to the limited diffusion under the ribs. On the contrary, the potential field applied by the

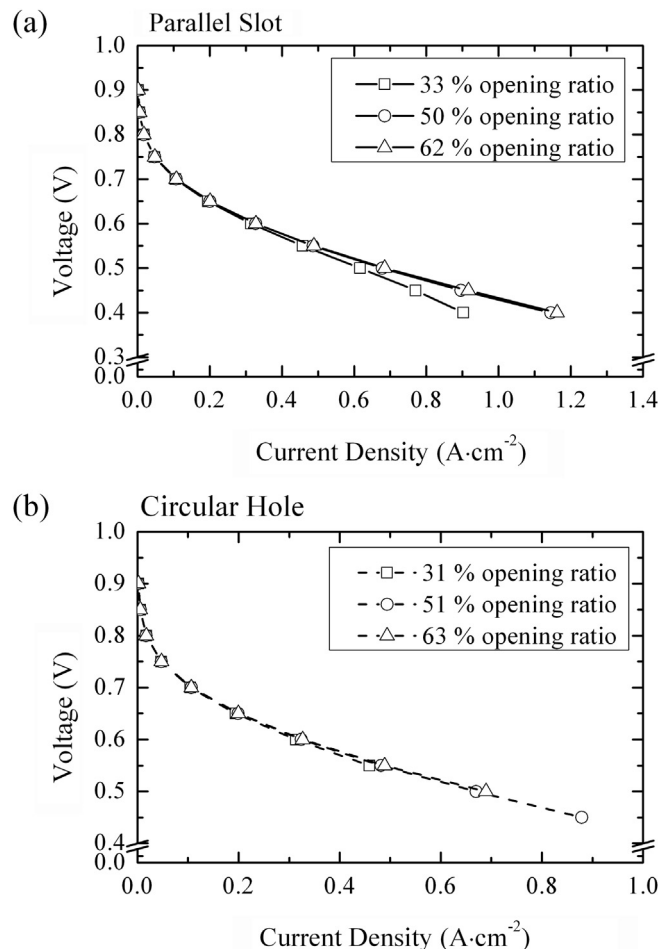


Fig. 9. The polarisation curves of the cell using (a) a parallel slot flow field design with opening ratios of 33%, 50% and 62% and (b) a circular hole flow field design with opening ratios of (a) 31%, (b) 51% and (c) 63%.

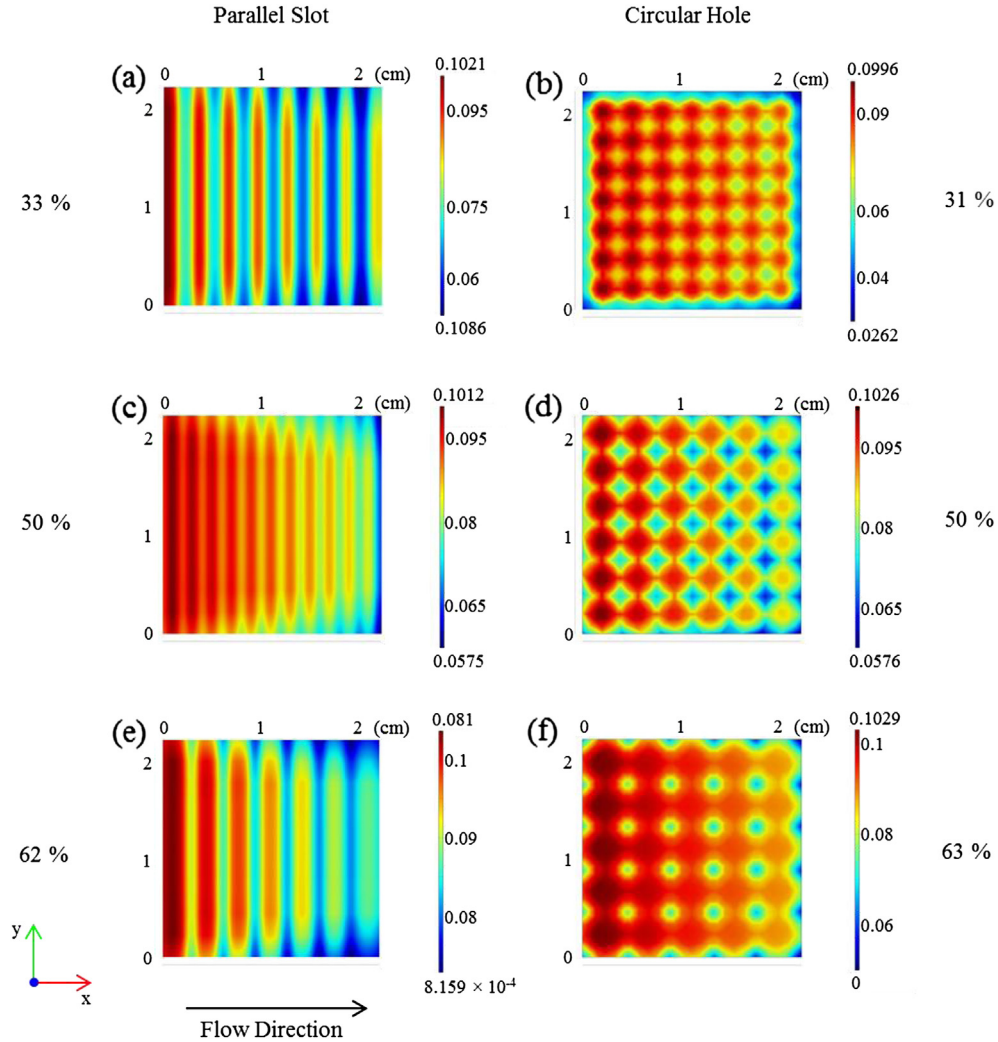


Fig. 10. The molar fractions of oxygen at the membrane–electrode interface for parallel slot flow fields of opening ratios (a) 33%, (c) 50%, (e) 62% and circular hole channel flow fields with opening ratios of (b) 31%, (d) 51% and (f) 63%.

current collector with an opening ratio of 62% has a more concentrated effect on the area beneath the ribs due to the greater distance between them, which causes a more prominent depletion of oxygen under each rib (Fig. 10). Given that the mole fraction of water exceeds the saturation pressure of water vapour in the electrode, the presence of water droplets could result in flooding without a sufficient mechanism for removal of excess water. However, the model is limited in that it cannot capture this phenomenon due to its single-phase nature. The parallel slot flow field with an opening ratio of 50% shows the most even distribution of oxygen (Fig. 10), indicating that a fine balance exists in the ratio of channel width to rib width for a parallel slot design.

Taking into account that the parallel slot flow field design shows the most promising electrochemical performance, the mole fractions of oxygen and water and temperature distribution were investigated at the central plane of the cell along the x -axis between the 6.15 mm and 16.15 mm for a cell length of 22.3 mm, which is equivalent to the centre length of 10 mm of the cell at the potentials 0.8 V, 0.6 V and 0.4 V (Fig. 11). As the opening ratios vary, the density of channels and lands changes; this is immediately noticeable in the number of peaks/troughs observed in the figure for each.

At 0.8 V, the mole fractions of oxygen and water lie within a similar range of values for each opening ratio due to the limited

cathodic reactivity present as seen by the small current densities present. However, the difference between the values in the electrode at the centre of the channel compared to the centre of the rib becomes more pronounced for all of the opening ratios and increasing current density. Moreover, the rise in temperature is directly proportional to an increase in the opening ratio and a decrease in potential. As the availability of oxygen in the cathode increases, the current density produced in the cell is greater resulting in elevated temperatures. This trend is most visible in the cell with an opening ratio of 62%. Specifically, it can be seen that with an opening ratio of 33% the cathode is depleted of oxygen under the ribs at 0.4 V as the mole fraction falls to close to zero. Using an opening ratio of 62% provides a greater availability of oxygen to the cathode in the channel region; however, it is significantly consumed in the area under the rib, as indicated by the troughs, reaching a low value of approximately 8.9×10^{-3} at 0.4 V. The opening ratio of 62% also demonstrates a better removal of water at 0.4 V, shown by the lower mole fractions of water in a range of 0.55–0.61, in comparison to the other two opening ratios, which could be contributed to greater channel area that allows for accessibility of flow from the plenum to remove water.

Overall, an opening ratio of 50% shows the most even distribution of species and heat. The fluctuation in values in the cathode between the areas under the channels and the ribs shows the

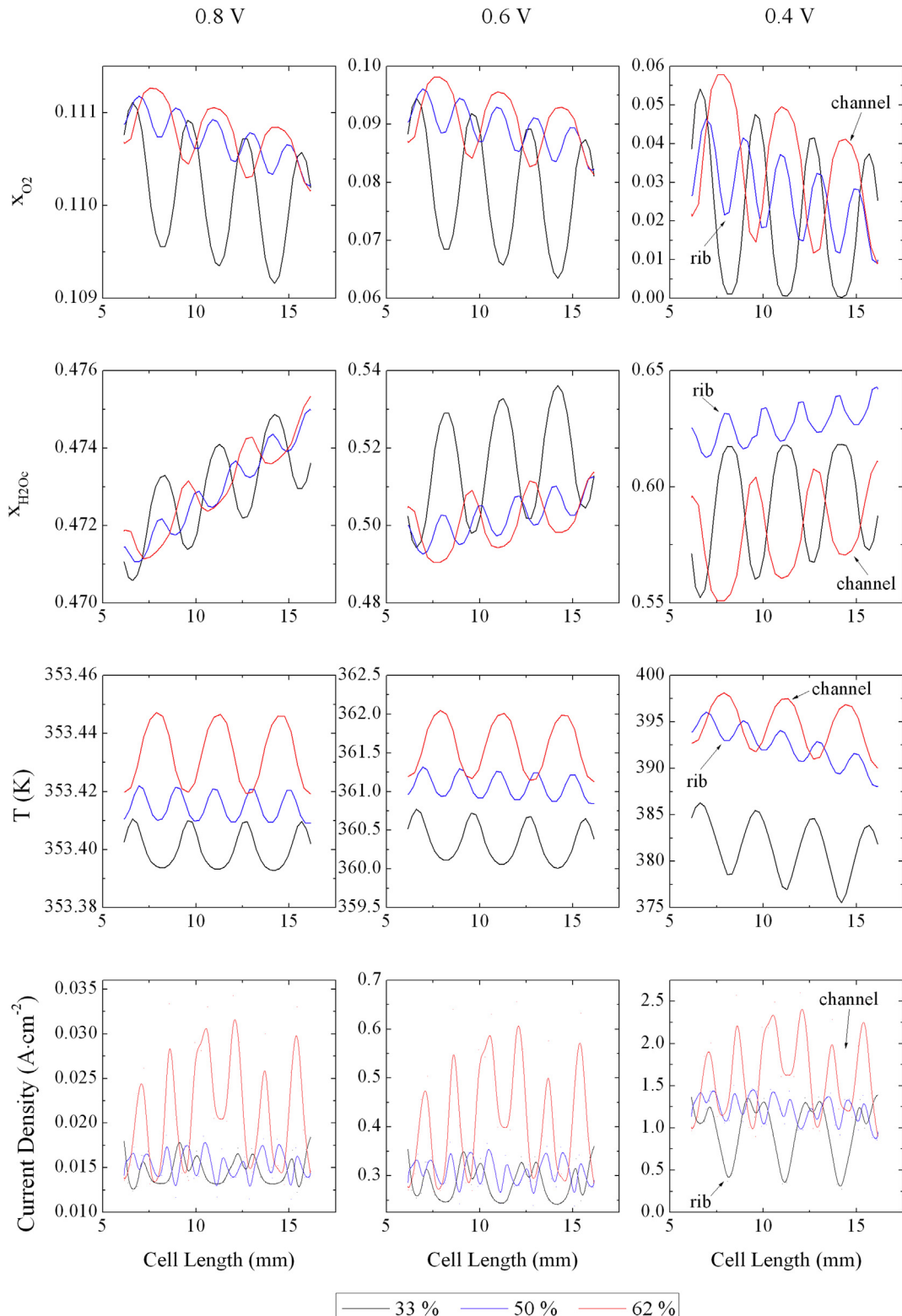


Fig. 11. Mole fractions of oxygen and water and temperature in the cathode at potentials of 0.8 V, 0.6 V and 0.4 V for opening ratios of (a) 33%, (b) 50% and (c) 62%. The peaks and troughs shown represent the centres of the channels and ribs as specified in the figures.

smallest range. Furthermore, it shows the least potential for oxygen depletion under the ribs in comparison to the other opening ratios. More importantly, a mechanism for removal of water is necessary as the water increasingly accumulates both under the ribs and the channels along the length of the cell.

4.4. Parametric study of inlet feed humidification

The closed-plenum parallel slot channel PCB current collector was modelled using various levels of humidification for the inlet feed. Four cases were considered: 100% relative humidity for both

the anode and cathode, 50% relative humidity (RH) for the anode and 100% RH for the cathode, 100% RH for the anode and 50% RH for the cathode and 50% RH for both the anode and cathode. Fig. 12 shows the polarisation curves for these four scenarios.

The water content of the anode feed has the greatest influence on the performance in all four cases considered. The performance of the cell at a lower anodic relative humidity begins to decrease at current densities above 0.1 A cm^{-2} . Reducing the relative humidity of the anode feed prevents sufficient hydration of the membrane causing the resistance of the membrane to increase, which is visible as a severe Ohmic loss in the polarisation curves for both cases of 50% anodic relative humidity. However, the cell operates slightly better with relative humidity of 50% for both the anode and the cathode as the molar concentration of oxygen in the cathode is higher than that of the cell when operating with a 50% anodic RH and 100% cathodic RH. In contrast, reducing the relative humidity of the cathode feed slightly improves performance. The lower humidification of the cathode feed results in a higher concentration of oxygen, which increases cell performance. Furthermore, the model predicts that operating at a lower cathodic relative humidity prevents the risk of flooding in the cathode, as the mole fraction in the cathode remains below the saturation pressure of water, varying between 0.276 and 0.352. Given that the cell cathode flooded during the experimental validation in Section 4.2, this observation is promising as it shows that better water management can possibly prevent flooding during prolonged use.

5. Conclusions

A detailed single-phase, three-dimensional model was constructed to investigate the effect of open-plenum current collector designs on the performance of PEM fuel cells. All major transport phenomena were accounted for through the use of electrochemical, mass, momentum and heat balances within the flow channels, gas diffusion layers, electrodes and electrolyte.

The model demonstrates that the parallel slot and circular hole channel flow field have similar performance across the range of cell voltages investigated. Specifically, based on a sensitivity analysis of the opening ratio of the channels, the parallel slot channel design consistently outperforms the circular hole channel design and shows the best species and temperature distribution in the MEA at

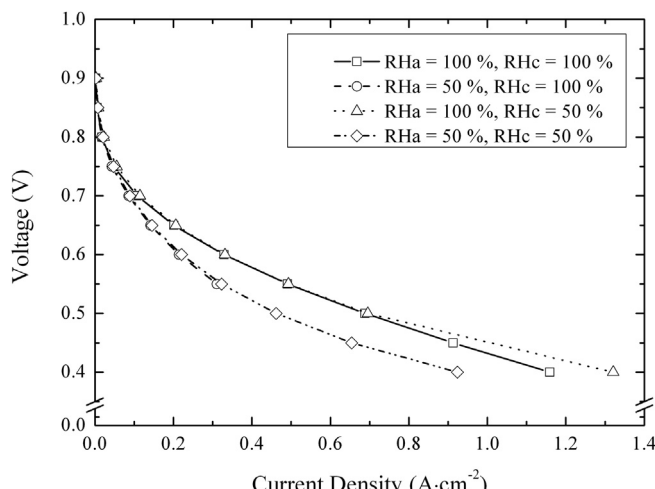


Fig. 12. Polarisation curves of the closed-plenum parallel slot channel cell with an opening ratio of 50% at inlet feeds with relative humidities of (a) 100% for both the anode and cathode, (b) 50% for the anode and 100% for the cathode, (c) 100% for the anode and 50% for the cathode and (d) 50% for both the anode and cathode.

50% opening ratio. Forced convection in a conventional parallel slot flow field provides a better distribution of species and heat, but provides only a small improvement in performance in comparison to a closed-plenum arrangement. Additionally, the performance is not limited by the current being removed laterally from the cell but is governed by the local oxygen concentration in the catalyst layer.

Modelling and experimental results also indicate that the closed-plenum cell is significantly prone to flooding and overheating. The high cathodic reactivity results in high water content in the porous layers, resulting in potential flooding. Reducing the relative humidity of the anode limits performance by reducing the hydration of the membrane. However, reducing the relative humidity of the cathode feed to 50% shows an improvement in performance and prevents the risk of flooding in the cathode observed during experimentation. The model suggests that the FR4 layer of the PCB has an insulating effect on the cell, causing elevated temperatures. The use of PCBs with higher thermal conductivity or cooling methods is necessary to prevent drying of the membrane and loss of performance over time due to thermal stress.

The closed-plenum cell, particularly with a parallel slot channel design, shows potential for use in various applications due to its high performance. However, the issues of flooding and overheating must be addressed using suitable humidification cooling and heating strategies in order to achieve and maintain this performance.

Acknowledgements

The authors would like to acknowledge the EPSRC (EP/G04483X/1) for supporting all of the authors on this paper and the EPSRC Supergen Fuel Cells program (EP/G030995/1) for supporting Brett and Kucernak.

Nomenclature

<i>a</i>	activity
<i>C</i>	molar concentration (mol m^{-3})
<i>c_p</i>	specific heat ($\text{J kg}^{-1} \text{K}^{-1}$)
<i>D</i>	diffusivity ($\text{m}^2 \text{s}^{-1}$)
<i>F</i>	Faraday's constant (C mol^{-1})
<i>i</i>	current density (A m^{-2})
<i>i₀</i>	exchange current density (A m^{-2})
<i>k</i>	thermal conductivity ($\text{W m}^{-1} \text{K}^{-1}$)
<i>L</i>	length (m)
<i>M</i>	molecular mass (kg mol^{-1})
<i>n</i>	electron number
<i>nd</i>	net drag coefficient
<i>p</i>	pressure (atm)
<i>P_{sat}</i>	saturation pressure of water vapour (atm)
<i>R</i>	universal gas constant ($8.314 \text{ J mol}^{-1} \text{ K}^{-1}$)
<i>R_i</i>	reaction term of species <i>i</i>
<i>S</i>	source term of governing equations
<i>t</i>	thickness (m)
<i>T</i>	temperature (K)
u	velocity vector (m s^{-1})
<i>V</i>	cell voltage (V)
<i>w</i>	mass fraction
<i>x</i>	molar fraction

Symbols

α	net water transport coefficient
ρ	density (kg m^{-3})
μ	viscosity ($\text{m}^2 \text{s}^{-1}$)
ε	porosity

ΔS	entropy change ($\text{J mol}^{-1} \text{K}^{-1}$)
η	overpotential (V)
λ	water content in the membrane
σ	conductivity (S m^{-1})

Subscripts

a	anode
c	cathode
Cu	copper
e	electrode
FP	flow plenum
GDL	gas diffusion layer
in	inlet
m	membrane (ionic phase)
oc	open circuit
PCB	printed circuit board
s	solid (electronic phase)
H_2O	water

References

- [1] D. Brett, N. Brandon, *Fuel Cell Rev.* 2 (2005) 15–23.
- [2] D.J.L. Brett, N.P. Brandon, *J. Fuel Cell Sci. Technol.* 4 (2007) 29–44.
- [3] D.M. Bernardi, M.W. Verbrugge, *J. Electrochem. Soc.* 139 (1992) 2477–2491.
- [4] T. Berning, D.M. Lu, N. Djilali, *J. Power Sources* 106 (2002) 284–294.
- [5] S.H. Ge, B.L. Yi, *J. Power Sources* 124 (2003) 1–11.
- [6] V. Gurau, H.T. Liu, S. Kakac, *AIChE J.* 44 (1998) 2410–2422.
- [7] G.H. Guvelioglu, H.G. Stenger, *J. Power Sources* 147 (2005) 95–106.
- [8] J.J. Hwang, *J. Power Sources* 164 (2007) 174–181.
- [9] H. Meng, *J. Power Sources* 164 (2007) 688–696.
- [10] T.E. Springer, T.A. Zawodzinski, S. Gottesfeld, *J. Electrochem. Soc.* 138 (1991) 2334–2342.
- [11] W.Q. Tao, C.H. Min, X.L. Liu, Y.L. He, B.H. Yin, W. Jiang, *J. Power Sources* 160 (2006) 359–373.
- [12] S. Um, C.Y. Wang, K.S. Chen, *J. Electrochem. Soc.* 147 (2000) 4485–4493.
- [13] N. Vasileiadis, D.J.L. Brett, V. Vesovic, A.R. Kucernak, E. Fontes, N.P. Brandon, *J. Fuel Cell Sci. Technol.* 4 (2007) 336–344.
- [14] M. Wohr, K. Bolwin, W. Schnurnberger, M. Fischer, W. Neubrand, G. Eigenberger, *Int. J. Hydrogen Energy* 23 (1998) 213–218.
- [15] J.S. Yi, T.V. Nguyen, *J. Electrochem. Soc.* 145 (1998) 1149–1159.
- [16] T.F. Fuller, J. Newman, *J. Electrochem. Soc.* 140 (1993) 1218–1225.
- [17] G.H. Guvelioglu, H.G. Stenger, *J. Power Sources* 163 (2007) 882–891.
- [18] Z.X. Liu, Z.Q. Mao, C. Wang, *J. Power Sources* 158 (2006) 1229–1239.
- [19] S. Mazumder, J.V. Cole, *J. Electrochem. Soc.* 150 (2003) A1503–A1509.
- [20] S. Mazumder, J.V. Cole, *J. Electrochem. Soc.* 150 (2003) A1510–A1517.
- [21] R. O'Hare, T. Fabian, S. Litster, F.B. Prinz, J.G. Santiago, *J. Power Sources* 167 (2007) 118–129.
- [22] M. Matian, A. Marquis, D. Brett, N. Brandon, *Proc. Inst. Mech. Eng. Part A J. Power Energy* 224 (2010) 1069–1081.
- [23] M. Matian, A. Marquis, N. Brandon, *Int. J. Hydrogen Energy* 36 (2011) 6051–6066.
- [24] A.P. Sasmito, E. Birgersson, A.S. Mujumdar, *Int. J. Therm. Sci.* 54 (2012) 242–252.
- [25] Y. Tabuchi, T. Shiomi, O. Aoki, N. Kubo, K. Shinohara, *Electrochim. Acta* 56 (2010) 352–360.
- [26] A. Kumar, R.G. Reddy, *J. Power Sources* 113 (2003) 11–18.
- [27] P.M. Kumar, A.K. Kolar, *Int. J. Therm. Sci.* 49 (2010) 844–857.
- [28] J. Lobato, P. Canizares, M.A. Rodrigo, F.J. Pinar, E. Mena, D. Ubeda, *Int. J. Hydrogen Energy* 35 (2010) 5510–5520.
- [29] T.V. Nguyen, *J. Electrochem. Soc.* 143 (1996) L103–L105.
- [30] B.P.M. Rajani, A.K. Kolar, *J. Power Sources* 164 (2007) 210–221.
- [31] R. Rosenthal, F. Arbab, G.K. Moghaddam, *Renew. Energy* 41 (2012) 86–95.
- [32] A. Schmitz, C. Ziegler, J.O. Schumacher, M. Tranitz, E. Fontes, C. Hebling, *Fuel Cells* 4 (2004) 358–364.
- [33] C.T. Wang, Y.C. Hu, P.L. Zheng, *Appl. Energy* 87 (2010) 1366–1375.
- [34] J.Y. Wang, *Int. J. Hydrogen Energy* 35 (2010) 5498–5509.
- [35] X.D. Wang, Y.Y. Duan, W.M. Yan, *J. Power Sources* 172 (2007) 265–277.
- [36] X.D. Wang, Y.Y. Duan, W.M. Yan, *J. Power Sources* 173 (2007) 210–221.
- [37] X.D. Wang, Y.Y. Duan, W.M. Yan, X.F. Peng, *Electrochim. Acta* 53 (2008) 5334–5343.
- [38] X.D. Wang, Y.Y. Duan, W.M. Yan, X.F. Peng, *J. Power Sources* 175 (2008) 397–407.
- [39] X.D. Wang, Y.Y. Duan, W.M. Yan, F.B. Weng, *J. Power Sources* 176 (2008) 247–258.
- [40] X.D. Wang, Y.X. Huang, C.H. Cheng, J.Y. Jang, D.J. Lee, W.M. Yan, A. Su, *Electrochim. Acta* 54 (2009) 5522–5530.
- [41] X.D. Wang, X.X. Zhang, W.M. Yan, D.J. Lee, A. Su, *Int. J. Hydrogen Energy* 34 (2009) 3823–3832.
- [42] X.D. Wang, Y.Y. Duan, W.M. Yan, D.J. Lee, A. Su, P.H. Chi, *J. Power Sources* 193 (2009) 684–690.
- [43] X.D. Wang, W.M. Yan, Y.Y. Duan, F.B. Weng, G.B. Jung, C.Y. Lee, *Energy Convers. Manage.* 51 (2010) 959–968.
- [44] X.D. Wang, Y.X. Huang, C.H. Cheng, J.Y. Jang, D.J. Lee, W.M. Yan, A. Su, *Int. J. Hydrogen Energy* 35 (2010) 4247–4257.
- [45] X.D. Wang, X.X. Zhang, W.M. Yan, D.J. Lee, A. Su, *Electrochim. Acta* 55 (2010) 4926–4934.
- [46] W.C. Weng, W.M. Yan, H.Y. Li, X.D. Wang, *J. Electrochem. Soc.* 155 (2008) B877–B886.
- [47] J.S. Yi, T. Van Nguyen, *J. Electrochem. Soc.* 146 (1999) 38–45.
- [48] W. Ying, T.H. Yang, W.Y. Lee, J. Ke, C.S. Kim, *J. Power Sources* 145 (2005) 572–581.
- [49] W. Ying, J. Ke, W.Y. Lee, T.H. Yang, C.S. Kim, *Int. J. Hydrogen Energy* 30 (2005) 1351–1361.
- [50] W. Ying, Y.J. Sohn, W.Y. Lee, J. Ke, C.S. Kim, *J. Power Sources* 145 (2005) 563–571.
- [51] C. Ziegler, A. Schmitz, M. Tranitz, E. Fontes, J.O. Schumacher, *J. Electrochem. Soc.* 151 (2004) A2028–A2041.
- [52] T. Berning, N. Djilali, *J. Power Sources* 124 (2003) 440–452.
- [53] S. Kjelstrup, M.O. Coppens, J. Pharoah, P. Pfeiffer, *Energy Fuels* 24 (2010) 5097–5108.
- [54] N. Karst, V. Faucheu, A. Martinent, P. Bouillon, J.Y. Laurent, F. Druart, J.P. Simonato, *J. Power Sources* 195 (2010) 1156–1162.
- [55] W.H.J. Hogarth, J.B. Benziger, *J. Electrochem. Soc.* 153 (2006) A2139–A2146.
- [56] R. O'Hare, D. Braithwaite, W. Hermann, S.J. Lee, T. Fabian, S.W. Cha, Y. Saito, F.B. Prinz, *J. Power Sources* 124 (2003) 459–472.
- [57] J.Y. Cao, Z.Q. Zou, Q.H. Huang, T. Yuan, Z.L. Li, B.J. Xia, H. Yang, *J. Power Sources* 185 (2008) 433–438.
- [58] C. D'Urso, V. Baglio, V. Antonucci, A.S. Arico, S. Specchia, U.A. Icardi, G. Saracco, C. Spinella, G. D'Arrigo, *Int. J. Hydrogen Energy* 36 (2011) 8088–8093.
- [59] L.G. Feng, W.W. Cai, C.Y. Li, J. Zhang, C.P. Liu, W. Xing, *Fuel* 94 (2012) 401–408.
- [60] Z. Guo, A. Faghri, *J. Power Sources* 160 (2006) 1183–1194.
- [61] Y.D. Kuan, S.M. Lee, M.F. Sung, *J. Fuel Cell Sci. Technol.* 6 (2009).
- [62] Y.D. Kuan, J.Y. Chang, S.M. Lee, *J. Power Sources* 196 (2011) 717–728.
- [63] M. Shen, S. Walter, L. Dovat, M.A.M. Gijs, *Microelectron. Eng.* 88 (2011) 1884–1886.
- [64] N. Bussajarn, H. Ming, K.K. Hoong, W.Y.M. Stephen, C.S. Hwa, *Int. J. Hydrogen Energy* 34 (2009) 7761–7767.
- [65] A. Parthasarathy, S. Srinivasan, A.J. Appleby, C.R. Martin, *J. Electrochem. Soc.* 139 (1992) 2530–2537.
- [66] C. Yang, P. Costamagna, S. Srinivasan, J. Benziger, A.B. Bocarsly, *J. Power Sources* 103 (2001) 1–9.